JOURNAL OF PROPULSION AND POWER
Vol. 23, No. 2, March–April 2007

Single-Cycle Unsteady Nozzle Phenomena in Pulse Detonation Engines

Zachary C. Owens* and Ronald K. Hanson†
Stanford University, Stanford, California 94305

DOI: 10.2514/1.22415

A quasi-one-dimensional, Euler model with detailed finite-rate chemistry is used to conduct a parametric assessment of nozzle area ratio effects on the single-cycle performance of a pulse detonation engine. Using results from the parametric study, design criteria are suggested for evaluating optimal contraction and expansion nozzle area ratios. In particular, the optimal expansion area ratio is shown to be well-predicted by using isentropic theory and the time-averaged, head wall pressure as the stagnation condition. To validate the parametric analysis, three nozzle sections are fabricated and tested in a single-cycle pulse detonation engine facility. Time-resolved thrust and specific impulse (I_{sp}) measurements are made for each nozzle and compared to simulated results. Additionally, schlieren imaging is used to investigate the blowdown gasdynamics in each of the three nozzles. Comparisons between simulated and measured impulse data are addressed using insights gathered from the flow visualization. Resulting analysis indicates that multidimensional wave phenomena are important in nozzles with converging sections. Overprediction of I_{sp} by the model is attributed to deficiencies in accurately capturing the plateau pressure (P_3), as well as the inability to model the experimentally observed deflagration-to-detonation transition process. The relative contribution of each of these effects is quantified. Experimental measurements validate trends observed in the parametric study and reveal that an appropriately optimized diverging nozzle produces the largest single-cycle I_{sp}.

Nomenclature

A_{exit}/A_{throat}	=	expansion area ratio
A_{throat}/A_{tube}	=	contraction area ratio
A_i	=	species i
$[A_i]$	=	concentration of species i
E	=	energy per unit volume
$\boldsymbol{F}$	=	convective flux vector
F_x	=	thrust
g	=	gravitational acceleration
h	=	enthalpy per unit mass
I_{sp}	=	specific impulse
k_b	=	backward rate coefficient
k_f	=	forward rate coefficient
M	=	molecular weight
m	=	mass
nr	=	number of reaction equations
ns	=	number of species
p	=	pressure
P_{amb}	=	ambient pressure
P_{fill}	=	reactant fill pressure
P_{head}	=	head wall pressure
P_i	=	partial pressure of species i
$P_{o,avg}$	=	time-averaged P_{head}
P_{spark}	=	spark region pressure
P_{wall}	=	internal gauge wall pressure
P_3	=	plateau pressure
$\boldsymbol{Q}$	=	area-variation source term vector
R_i	=	specific gas constant for species i
S	=	flux surface
t	=	time
t_{cycle}	=	time from ignition until $P_{wall} = P_{amb}$
$\boldsymbol{U}$	=	state vector
u	=	axial velocity
v'_i	=	stoichiometric coefficient of reactant
v''_i	=	stoichiometric coefficient of product
$\boldsymbol{W}$	=	species production rate vector
Y_i	=	mass fraction of species i
ρ	=	mass density

Presented as Paper 3649 at the 40th AIAA/ASME/SAE/ASEE Joint Propulsion Conference & Exhibit, Tucson, AZ, 10–13 July 2005; received 12 January 2006; revision received 14 August 2006; accepted for publication 15 August 2006.

*Graduate Student, Aeronautics & Astronautics, Building 520, Room 520 I. Student Member AIAA.

†Professor, Mechanical Engineering, Building 520, Room 520 E. Fellow AIAA.

I. Introduction

PULSE detonation engines are currently an active area of propulsion research due to their potential for increased performance and reduced mechanical complexity in comparison to more conventional chemical propulsion systems [1]. Although idealistic thermodynamic [2,3] and gasdynamic [4,5] analysis suggests the pulsed propulsion cycle can be more efficient than its steady-flow counterparts, it remains to be shown whether a practical device can be developed to exploit these inherent advantages. Critical to the success of the PDE concept is the implementation of a nozzle capable of efficiently converting as much of the thermal energy in the exhaust gases into usable propulsive force. Whereas optimal nozzle design for steady, constant pressure, propulsion systems is well established and relatively straightforward, the problem of designing nozzles for pulsed propulsion systems poses a significantly greater challenge due to the inherently unsteady flowfield.

Many previous computational and experimental PDE nozzle studies have been conducted and presented in the literature. A detailed literature review of work before 2002 was performed by Kailasanath [6,7], and more recent efforts have been chronicled by Wu et al. [2] and Cooper and Shepherd [8]. Topics of most recent interest that have been influential on the direction of this work include nozzle performance at reduced backpressures [8–10] and multicycle nozzle performance [2,11–14]. Several key nozzle design issues have arisen as a result of these most recent studies. Computational studies by Morris [9,10] and experiments conducted by Cooper and Shepherd [8] reveal that appropriately designed nozzles can provide increasing impulse enhancement over the straight-tube extension as the ambient pressure is decreased. Both

studies consider single-shot operation where reactant fill pressure is held constant with respect to a variable ambient condition. Consequently, multicycle PDEs will only be able to achieve these large impulse enhancements provided a method of maintaining a high fill-to-ambient pressure ratio between cycles is identified. Yungster [12] also comments on the importance of maintaining high fill pressures between cycles as high expansion ratio nozzles can lead to significant overexpansion losses during purging and refilling. Wu et al. [2] simulated a multicycle, airbreathing PDE and demonstrated the use of a nozzle with a 0.56 contraction ratio as a means of maintaining higher fill pressure. Additionally, they noted that the convergent section had the benefit of decreasing the Mach number of the reactants between cycles. The performance losses associated with initiating detonations in nonquiescent reactants has been studied previously by Guzik and Harris [15] and Witenberger and Shepherd [5].

Previous studies were successful in identifying the most important criteria governing unsteady nozzle performance. This list of criteria includes expansion area ratio, contraction area ratio, nozzle contour (conical, bell, plug, etc.), partial fill effects, and nozzle pressure ratio. In this paper we choose to focus on the most fundamental geometric criteria in this list: nozzle expansion and contraction ratio. In a steady, constant pressure, propulsion system, the nozzle throat is chosen to maintain chamber pressure while minimizing stagnation pressure losses. In an unsteady PDE the contraction ratio has the additional role of controlling cycle frequency (blowdown time) and the reflecting wave system which is established in the combustion chamber [16]. As in the case of the steady system, the expansion ratio should be chosen to optimally expand the combustion products to ambient pressure. However, unlike the steady system, the stagnation pressure in the PDE chamber is time variant, and this must be appropriately accounted for when choosing an optimal expansion ratio.

In this work a chemically reacting, quasi-one-dimensional Euler code was developed to parametrically assess the role of the contraction and expansion area ratios on single-cycle PDE performance. This work is unique in that a large number of nozzles (16) are simulated and compared to reveal area ratio effects. From these results guidelines are derived for choosing optimal area ratios for an unsteady PDE. Considerations for multicycle PDEs operating at reduced ambient pressures will also be addressed. Guided by the results of the parametric study, three nozzles were built and tested in an interchangeable, two-dimensional nozzle facility. Time-resolved impulse measurements were made in each nozzle and were spatially resolved on each thrust surface (e.g., head wall, converging section, diverging section). Comparisons of the experiments to computational results are made and discrepancies are addressed. To further aid in assessing the ability of the computations to accurately predict unsteady nozzle blowdown phenomena, schlieren images of the blowdown process in each of the three nozzles are also presented. These images of PDE nozzle gasdynamics are the first available in the literature.

The emphasis of the current work is on single-cycle, unsteady nozzle performance and flow phenomena. It is well understood in the PDE community that multicycle and single-cycle nozzle optimization studies do not produce convergent results. Nevertheless, the utility of the single-cycle results presented in this paper is to illuminate generalized unsteady nozzle behavior which can then be extended to more practical multicycle systems. The results presented herein should also heighten the readers' awareness of the importance of comparing optimally designed versions of each nozzle type. For instance, with a limited number of data points corresponding to arbitrarily designed diverging nozzles, a general conclusion may be drawn that straight-tube extensions are superior to diverging nozzles. However, the opposite is likely to be the case if the diverging nozzles' expansion ratio is chosen optimally.

II. Computational Model

The unsteady, compressible, quasi-one-dimensional Euler equations are used as an approximate model of the gasdynamics in this study. Real detonation waves exhibit multidimensional structures and create complex systems of reflecting waves when propagating through variable area nozzles. Nozzle separation is also an inherently viscous, multidimension phenomenon that cannot be simulated with this equation set. Nevertheless, whereas the model will be inadequate for capturing these multidimensional, viscous flow features, it will provide a computationally inexpensive platform from which to conduct parametric nozzle studies. Additionally, quasi-one-dimensional models have been shown in the past to predict PDE flowfield variables in good agreement with experimental data [16–18]. The equation set, accounting for finite-rate chemical reactions, can be written as follows:

$$\frac{\partial \boldsymbol{U}}{\partial t} + \frac{1}{S}\frac{\partial \boldsymbol{FS}}{\partial x} = \boldsymbol{Q} + \boldsymbol{W} \tag{1}$$

The state vector, flux vector, area-variation source term and chemical source term are given by

$$\boldsymbol{U} = \begin{bmatrix} \rho \\ \rho u \\ E \\ \rho Y_1 \\ \rho Y_2 \\ \vdots \\ \rho Y_{\mathrm{ns}-1} \end{bmatrix}, \quad \boldsymbol{F} = \begin{bmatrix} \rho u \\ \rho u^2 + p \\ (E+p)u \\ \rho u Y_1 \\ \rho u Y_2 \\ \vdots \\ \rho u Y_{\mathrm{ns}-1} \end{bmatrix}, \quad \boldsymbol{Q} = \begin{bmatrix} 0 \\ \frac{p}{S}\frac{\partial S}{\partial x} \\ 0 \\ 0 \\ 0 \\ \vdots \\ 0 \end{bmatrix}$$

$$\boldsymbol{W} = \begin{bmatrix} 0 \\ 0 \\ 0 \\ \dot{w}_1 \\ \dot{w}_2 \\ \vdots \\ \dot{w}_{\mathrm{ns}-1} \end{bmatrix} \tag{2}$$

The fluid is considered to be mixture of thermally perfect gases and the equation of state can be written as shown in Eq. (3). Equation (4) represents the volumetric energy content of the gas mixture.

$$p = \sum_{i=1}^{\mathrm{ns}} p_i = \rho\left(\sum_{i=1}^{\mathrm{ns}} Y_i R_i\right) T = \rho R T \tag{3}$$

$$E = -p + \rho\left(\frac{u^2}{2} + h\right) \tag{4}$$

The chemical source terms in Eq. (2) are computed with the aid of a chemical mechanism which consists of a set of nr elementary chemical reactions of the form

$$\sum_{i=1}^{\mathrm{ns}} = v'_{i,n} A_i \Leftrightarrow \sum_{i=1}^{\mathrm{ns}} v''_{i,n} A_i \tag{5}$$

The mass production term for each species A_k can be evaluated by summing the creation and destruction rates in each of the relevant nr reactions:

$$\dot{w}_k = M_k \sum_{n=1}^{\mathrm{nr}} \left(v''_{k,n} - v'_{k,n}\right)\left[k_f \prod_{i=1}^{\mathrm{ns}} [A_i]^{v'_{i,n}} - k_b \prod_{i=1}^{\mathrm{ns}} [A_i]^{v''_{i,n}}\right] \tag{6}$$

For each elementary reaction k_f is computed using the conventional Arrhenius relationship, whereas the backward reaction rate is computed using k_f and the equilibrium constant.

To obtain maximum versatility, the flow solver uses the CHEMKIN [19] gas-phase subroutine library and thermodynamic database. This permits existing chemical mechanisms and species data written in the CHEMKIN format to be easily integrated into the flow solver. In this study we consider stoichiometric C_2H_4/O_2 and use a slightly modified version of the 21-species, 33-reaction reduced

mechanism developed by Varatharajan and Williams [20]. Per the suggestion of Morris (in Owens et al. [16]) the 33 forward reactions described in the original mechanism are made reversible. For the grid resolution used throughout this study the level of detail present in the chemical mechanism is somewhat superfluous; however, this mechanism provides a reliable way to reach equilibrium without having to tune any problem-dependent variables as would be the case for a global treatment of the reaction kinetics. Additionally, the use of a chemical mechanism that has been validated over a wide range of conditions [20] provides a more robust platform from which to make quantitative performance comparisons with experimental data.

Before solving Eq. (1) it is first split using Strang's [21] second-order, time-step-splitting procedure. In this procedure Eq. (1) is recast into two equations: one which describes fluid convection with no chemical reaction as shown in Eq. (7), and the other which describes chemical reaction in a motionless fluid as shown in Eq. (8).

$$\frac{\partial \boldsymbol{U}}{\partial t} + \frac{1}{S}\frac{\partial \boldsymbol{FS}}{\partial x} = \boldsymbol{Q} \tag{7}$$

$$\frac{\mathrm{d}\boldsymbol{U}}{\mathrm{d}t} = \boldsymbol{W} \tag{8}$$

Equation (7) is discretized over the computational domain in finite-volume form and convective fluxes at cell interfaces are computed using a third-order, essentially nonoscillatory (ENO)-Roe scheme with an entropy fix [22]. It should be noted that the chosen ENO scheme only achieves a third-order convergence rate on smooth flows which lack discontinuities and is at best first-order convergent otherwise [23]. This is the case with all higher-order shock capturing methods; nevertheless, the advantages of these schemes for flows containing both discontinuities and complex solution features have been demonstrated in the literature [24]. The left and right eigenvectors of the flux Jacobian, required to move into and out of characteristic space in the ENO algorithm, are evaluated using Roe averages at the cell interfaces as described in [25]. The fluid convection equation is advanced in time using a third-order, explicit, total variation diminishing Runge–Kutta algorithm [26]. The chemical reaction equation, Eq. (8), is a stiff system of ordinary differential equations. This system is solved using the publicly available LSODE package. To couple Eqs. (7) and (8), the solver first advances the chemical reactions by a half time step, followed by a full time step of fluid convection, proceeded by a second half time step of chemical reaction. In operator notation this looks like

$$\boldsymbol{U}^{n+1} = L_{\mathrm{chem}}^{\Delta t/2} L_{\mathrm{conv}}^{\Delta t} L_{\mathrm{chem}}^{\Delta t/2} \boldsymbol{U}^{n} \tag{9}$$

Because the chemical reaction steps are separate from the fluid convection step, it is convenient that the gas chemistry can be frozen simply by removing the chemical reaction operators in Eq. (9). In the simulations presented here using the 21-species, 33-reaction mechanism, the fluid convection step requires a small fraction of the computational expense required to update the stiff chemical reaction equations.

For the single-pulse calculations considered in this work a reflective boundary condition is used at the tube head wall. A characteristic [27], subsonic inflow boundary condition can also be activated at the head wall to simulate purging and refilling, although this capability is not used in this work. An analogous characteristic outflow boundary condition is used at the exit plane. For the case of subsonic outflow, ambient pressure is specified directly at the tube exit. The resulting effect of a zero-relaxation-length, one-dimensional boundary condition has been explored previously by Kailasanath and Patnaik [28]. In the case of the straight-tube configuration a choked flow constraint is imposed at the exit. Additional details regarding boundary condition implementation can be found in [16].

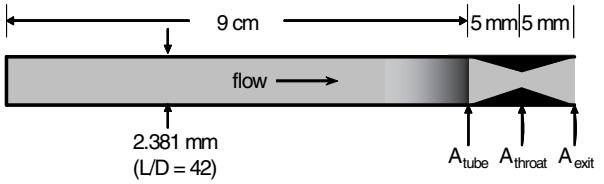

Fig. 1 Computational setup used for parametric analysis of area ratio effects. Tube length and nozzle length are fixed, whereas nozzle contraction and expansion area ratios are varied by changing the inlet and exit angles.

III. Area Ratio Effects on Nozzle Performance

A. Test Configuration

Using the model described in the preceding section, a parametric assessment of the effect of contraction and expansion area ratio on nozzle performance was conducted. Figure 1 depicts the test configuration used in this computational study. In all cases a stoichiometric mixture of C_2H_4/O_2 was used to fill the entire tube volume, including the nozzle section. The detonation was initiated directly using a 1 mm long region of high temperature and pressure gasses adjacent to the head wall as the spark region. For all cases the spark temperature was set to 3000 K, whereas the ratio of $P_{\mathrm{spark}}/P_{\mathrm{fill}}$ was fixed at 30. Using a fixed P_{spark} for all tested values of P_{fill} was avoided because at the lowest fill pressures a high P_{spark} value leads to highly overdriven detonations and has a nonnegligible effect on the resulting impulse.

For all fill pressures tested the model computes average detonation velocity to within 2.5% of the Chapman–Jouguet (CJ) value computed using STANJAN [29], and the pulsating nature of the wave speed is observed as described by Yungster and Radhakrishnan [30]. Chapman–Jouguet flow properties are reproduced nearly exactly at the highest tested fill pressures with maximum deviations on the order of 5% at the lowest fill pressure. Detonation formation and propagation are computed at a constant grid resolution of 0.1 mm. This grid resolution is too coarse to resolve the reaction zone, especially at high fill pressures, but shows high fidelity for reproducing the CJ state as indicated. The fully reacting equations are solved using 0.1 mm grid resolution until the detonation front has reached the nozzle entrance, at which point the chemistry is frozen throughout the entire domain, and the remainder of the blowdown is computed at 0.4 mm grid resolution. A grid refinement study was performed to identify the least number of grid points required to resolve the flowfield and accurately capture the CJ state.

The computed I_{sp} is evaluated based on the fuel and oxidizer mass occupying the thrust chamber up to the start of the nozzle section. Consequently, the fuel/oxidizer loading is the same for all nozzles cases evaluated at a given fill pressure. Equations (10) and (11) indicate how I_{pulse} and I_{sp} are defined throughout this work. In effect, the stoichiometric mixture of C_2H_4/O_2 occupying the nozzle section is isolated from the rest of the thrust chamber by a virtual diaphragm until detonation arrival. Because the chemistry is frozen after detonation arrival, the nozzle mixture does not combust and acts only as a tamper mass. As discussed in [9] the choice of gas composition for the nozzle tamper mass can have a small effect on the resulting impulse. However, for this study the nozzle fluid composition is invariant between cases and is not expected to affect the resulting trends.

$$I_{\mathrm{pulse}} = \int_0^{t_{\mathrm{cycle}}} F_x(t)\,\mathrm{d}t \tag{10}$$

$$I_{\mathrm{sp}} = \frac{I_{\mathrm{pulse}}}{m_{\mathrm{fuel+oxidizer}}\, g} \tag{11}$$

The choice to freeze the chemistry after detonation arrival at the nozzle entrance was done to avoid the computational expense of updating the chemical source terms throughout the blowdown.

Several runs were made to compare frozen cases to runs made with finite-rate kinetics occurring throughout the blowdown. In general, the inclusion of finite-rate kinetics in the blowdown has the effect of maintaining higher chamber temperatures due to its ability to capture exothermic recombination reactions. The extra energy release results in slightly higher chamber pressures which translate to increased I_{sp} values on the order of 5% for the cases tested. In this parametric study, the actual magnitude of the I_{sp} results are of secondary importance. The primary goal is to correctly reproduce trends resulting from changes in area ratio. The role of nozzle chemistry is expected to have the most substantial impact in nozzles with large expansion area ratios where inlet temperatures will be substantially higher than exit temperatures. In this study the simulated expansion ratios are low and occupy a narrow range, and thus the choice to freeze the chemistry during blowdown is expected to affect all nozzles equally and preserve the desired trends.

The nozzle used in the test configuration is a variable-area-ratio, conical, converging-diverging (CD) nozzle of fixed length as depicted in Fig. 1. A fixed nozzle length was employed to prevent the partial fill phenomena from becoming a competing variable. If the nozzle length were not constant then the performance of longer nozzles would benefit from the partial fill effect more so than shorter nozzles, and this would obscure the observation of area ratio influence. The contraction area ratio is adjusted by varying the convergent inlet angle, and the expansion area ratio is controlled similarly by varying the divergent exit angle. To minimize the impact of using a quasi-one-dimensional model, the nozzle half angles are kept small with the maximum never exceeding 6 deg. The tube L/D ratio was selected to replicate the experimental PDE facility which will be described shortly.

In this study, in contrast to previous single-cycle studies, the reactant fill pressure is decreased in parallel with the ambient pressure to simulate high-altitude flight conditions. In each case the reactant initial condition is set by equating the fill pressure to the ambient pressure while setting the fill temperature to 300 K. The single-cycle blowdown time is defined as the time between detonation initiation and the time at which the head wall of the PDE decays to ambient pressure. As discussed previously, multicycle simulations have revealed the difficulty in maintaining chamber pressures above the ambient value during refilling. Equating the fill pressure and ambient pressure was chosen to more closely approximate current multicycle operation. It should be emphasized that PDE performance increases substantially as the fill-to-ambient pressure ratio is increased [8,9].

Sixteen nozzles were considered in this study in addition to the straight-tube extension, which serves as a reference condition. The contraction area ratio for this set of nozzles varied between 0.4 and 1.0, representing maximum throat obstruction and no throat obstruction, respectively. The expansion area ratio was increased incrementally until an optimal point was identified for each contraction area ratio. The range of expansion ratios was not known a priori, and consequently the number and exact geometry of each nozzle in the test matrix was not predetermined. This process was repeated at five different fill pressures ranging from 1 atm down to 0.05 atm.

B. Simulation Results

In Fig. 2 single-cycle I_{sp} for stoichiometric C_2H_4/O_2 is plotted vs nozzle area ratio for the case of 1 atm fill pressure. The left-running axis shows nozzles with increasing expansion area ratio, whereas the right-running axis shows nozzles with a decreasing level of throat obstruction. The projection of each curve onto each of the three-axis planes is shown with a dashed line. The projection on the back-left surface illustrates very clearly that single-cycle I_{sp} decreases as throat obstruction increases. This effect occurs because the impulse loss incurred on the convergent section is generally larger then the increase in impulse incurred at the head due to wave reflections and increased blowdown time. The vertical separation between projections on the back-left plane reveal the effect of expansion area ratio. The three upper curves are very close to the optimal

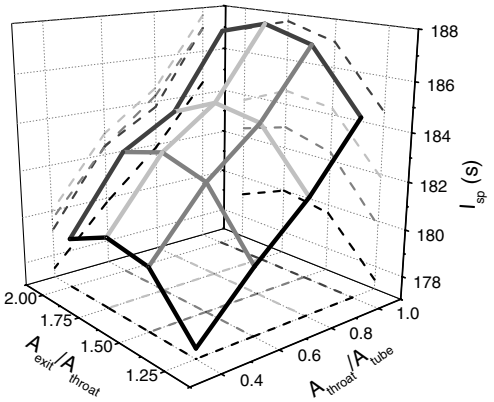

Fig. 2 Single-cycle I_{sp} vs area ratio. Reference I_{sp} for the straight-tube extension is 180.2 s. ($P_{fill} = P_{amb} = 1$ atm).

expansion area ratio, whereas the lower curve, representing $A_e/A_t = 1.25$, is underexpanded and has a decreased level of performance.

The parabolic shapes of the curves on the back-right surface reveal the optimal expansion area ratio for each nozzle configuration. Whereas there are not enough data points to refine this optimal value exactly, the approximate optimal expansion ratio is very close to 1.75 for all four contraction ratios illustrated. This reveals that optimal expansion area ratio is not a strong function of the level of throat obstruction. This point will be examined further shortly. Although expansion ratios above 2 are not shown, the downward slope will continue as performance drops due to overexpansion.

Losses due to overexpansion can be severe, especially at high backpressures, and without a carefully designed expansion ratio it may be concluded that straight tube is the preferred configuration. The reference straight-tube case for the 1 atm condition illustrated in Fig. 2 has an I_{sp} of 180.2 s. Figure 2 reveals that all optimally expanded nozzle configurations either match or exceed this level of performance. The straight tube will only show significant performance enhancement over nozzles with expansion ratios that deviate substantially from this optimal point. For instance, a purely diverging nozzle with an expansion ratio of 4 (not shown) produces a single-cycle I_{sp} of 168 s for the conditions of Fig. 2. This is 7% lower in performance then the straight-tube case, yet the optimally expanded diverging nozzle depicted in Fig. 2 outperforms the straight-tube case by 4%.

In Fig. 3 the normalized single-cycle blowdown time is plotted as a function of area ratio. Here, the blowdown times for each nozzle configuration have been normalized by the straight-tube blowdown time. The projection on the back-right surface of the plot reveals the high sensitivity of blowdown time to contraction area ratio. Nozzles with contraction area ratios of 0.4 take over twice as long to complete a single cycle relative to the straight-tube case. On the other hand, purely diverging nozzles have slightly shorter blowdown times than the straight-tube case. For multicycle PDEs, where operating frequency contributes to performance, cycle time is an important consideration. The projection on the back-left surface of Fig. 3 reveals that blowdown time is insensitive to expansion ratio.

Figures 2 and 3 portray the optimally expanded, diverging nozzle as the top performer because it attains the highest I_{sp} and has the shortest blowdown time. However, as indicated previously, a multicycle PDE will not operate efficiently unless the reactants can be combusted at high pressure and low Mach number. From this standpoint the purely diverging nozzle is the worst choice as its lack of a throat leads to higher velocities and lower chamber pressures at the end of a cycle. Ultimately, designing the contraction ratio for a multicycle PDE will be done as an iterative tradeoff between the single-cycle performances losses resulting from throat constriction vs the multicycle benefit of increasing the combustion efficiency by optimizing the state of the reactants before detonation initiation.

In designing the expansion area ratio for a steady nozzle, the optimal point can be found for a given ambient pressure using isentropic analysis, provided the stagnation pressure of the

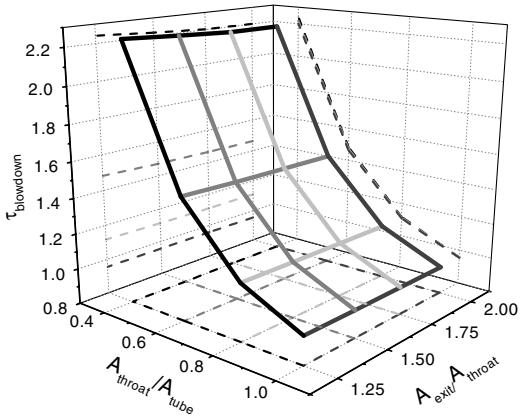

Fig. 3 Normalized single-cycle blowdown time vs area ratio. Blowdown times have been normalized by the straight-tube blowdown time. ($P_{\text{fill}} = P_{\text{amb}} = 1$ atm).

combustion chamber is known. A similar procedure can be done for the unsteady PDE, provided a suitable definition for the design stagnation pressure is identified. In this work the single-cycle, time-averaged head wall pressure is proposed for this purpose. This pressure is defined as indicated in Eq. (12). For multicycle PDEs a more suitable definition would involve averaging over the limit cycle which would be defined to include purging and refilling stages.

$$P_{o,\text{avg}} = \frac{\int_o^{t_{\text{cycle}}} P_{\text{head}}\, \mathrm{d}t}{t_{\text{cycle}}} \tag{12}$$

Using this definition, $P_{o,\text{avg}}$ has been plotted in Fig. 4 for each of the 16 different nozzle configurations at the 1 atm condition. Figure 4 indicates that $P_{o,\text{avg}}$ decreases as the level of throat obstruction increases. This may go against initial intuition; however, the effect is a result of the prolonged amount of time it takes the plateau pressure to relax back to the ambient condition for nozzles with increased throat obstruction. During this relaxation period the average head pressure is lower than the plateau condition (P_3), which dominates the early stages of the cycle. Consequently, configurations with the short blowdown times have higher $P_{o,\text{avg}}$ values which are closer to P_3 than configurations with long blowdown times. Figure 4 also reveals that the $P_{o,\text{avg}}$ is not sensitive to expansion area ratio. This is a convenience to the designer because it decouples the design stagnation pressure from the quantity being optimized.

With regard to Fig. 4, a general point can also be made that if the fill pressure is at least equal to the ambient pressure, then there will be some performance enhancement obtainable through the implementation of a nozzle. This is the case because $P_{o,\text{avg}}$ during a single cycle is necessarily higher then the ambient value as a result of detonative compression. This elevated stagnation pressure can always be expanded to some extent to extract additional performance. The level of performance augmentation that results from this expansion is directly proportional to $P_{o,\text{avg}}/P_{\text{amb}}$. This was indirectly shown in [8,9] where P_3 and P_{fill} were considered instead of $P_{o,\text{avg}}$. All three of these reference stagnation pressures are directly proportional to one another.

In the course of this study simulation data were generated to reproduce Figs. 2–4 at four additional fill pressure conditions extending down to 0.05 atm. The trends already discussed with regard to the 1 atm case apply to each of the cases investigated at lower pressures, and for this reason these plots will not be shown. Instead, to summarize the effects of reduced fill pressure, in Fig. 5 I_{sp} is plotted vs expansion ratio for a series of purely diverging nozzles operating at different fill pressures.

The first major conclusion to draw from Fig. 5 is that I_{sp} is directly proportional to fill pressure over the range shown. The optimized diverging nozzle at 1 atm fill pressure shows a 9% increase in I_{sp} performance over the optimized nozzle at 0.05 atm. The performance increase is directly attributable to the increased heat release occurring at higher pressures as a result of increased rate of exothermic recombination. It should be noted that a high pressure limit is expected to be reached as increased recombination leads to a state where radical species are dominated by major products. This effect was observed previously by Witenberger et al. [31]. The direct scaling of I_{sp} with P_{fill} below this high pressure limit again emphasizes the importance of maintaining high P_{fill} in multicycle operation. It should also be noted that the magnitude of the performance results in Fig. 5 would be shifted upwards if $P_{\text{fill}}/P_{\text{atm}}$ were greater than unity.

The second point to draw from Fig. 5 is that the optimal area ratio does not change substantially between the various pressure conditions. This is to be expected because optimal area ratio is primarily a function of $P_{\text{fill}}/P_{\text{atm}}$, which is held constant, and only minimally dependent on P_{fill} through the chemical recombination effect discussed previously. Consequently, it is expected that higher P_{fill} cases would have slightly higher optimal expansion area ratios and this expected trend is recovered in Fig. 5.

For the nozzle designer looking for a simple, first-order method of identifying optimal expansion area ratio it would be particularly convenient to be able to identify $P_{o,\text{avg}}$ without having to perform detailed CFD calculations. The most direct way of getting $P_{o,\text{avg}}$ is to measure it experimentally. Ideally, this would be done at a given contraction area ratio, as it has been shown that $P_{o,\text{avg}}$ is most sensitive to this parameter. Once $P_{o,\text{avg}}$ has been determined for a given contraction ratio an isentropic calculation can be performed to identify the optimal expansion area ratio. Alternatively, it is also possible to roughly estimate $P_{o,\text{avg}}$ for a straight-tube configuration based on Witenberger et al.'s analytic model [31]. The major uncertainty in using this analytic method arises in defining the duration of a single cycle, which is not explicitly treated in the model.

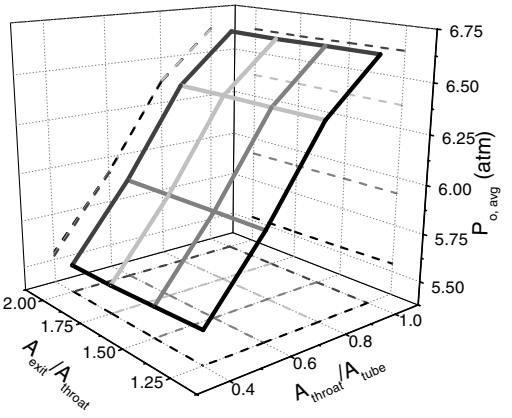

Fig. 4 $P_{o,\text{avg}}$ vs area ratio. Reference $P_{o,\text{avg}}$ for the straight tube is 6.53 atm. ($P_{\text{fill}} = P_{\text{amb}} = 1$ atm).

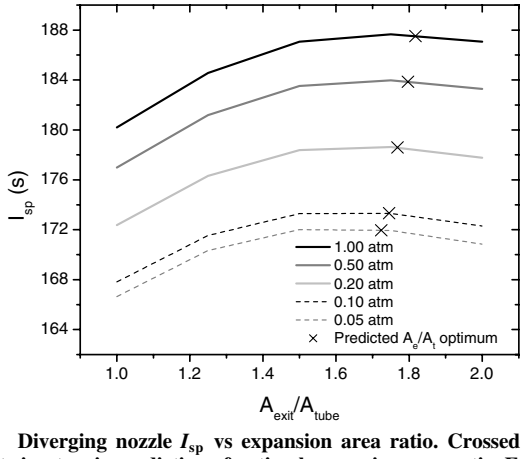

Fig. 5 Diverging nozzle I_{sp} vs expansion area ratio. Crossed points indicate isentropic prediction of optimal expansion area ratio. For each case $P_{\text{fill}} = P_{\text{amb}}$.

The crossed data points in Fig. 5 are an isentropic prediction of the optimal expansion ratio (not the I_{sp}), based on computed values of $P_{o,\text{avg}}$ for the straight tube evaluated at each fill pressure. The straight tube $P_{o,\text{avg}}$ is an appropriate reference case for the diverging nozzles shown in Fig. 5 because both configurations have the same contraction ratio. As evident, this simple analysis is able to predict the optimal expansion ratio to within the resolution of the computations. This type of simple analysis could be useful in providing a starting point for more sophisticated optimization procedures involving multidimensional CFD.

IV. Experimental Impulse Measurement and Schlieren Imaging

A. Test Configuration

To validate the trends discussed in the parametric study, three nozzle sections were fabricated for experimental testing. The first nozzle is a planar (2-D), CD nozzle with a contraction ratio of 0.4 and an expansion area ratio of 2.0. The second nozzle is a planar, diverging nozzle with an expansion area ratio of 2.0. Detailed drawings of both nozzle inserts are shown in Fig. 6. The exact optimal area ratios identified in the parametric study are not strictly applicable to the experimental facility because of differing geometry, initiation method, and filling strategies which will be discussed shortly. Nevertheless, an expansion ratio of 2 was chosen to be in close vicinity to the optimal point from the parametric study, and is sufficiently close to the true optimal point to recover the trends discussed in the preceding section. The third nozzle section is simply a square channel straight extension. All nozzles considered in these experiments were planar to allow schlieren imaging of the entire nozzle channel. The flow visualization is intended to aid in assessing the validity of using the proposed computational model and helps justify discrepancies between observed and simulated PDE performance.

1. PDE Facility Description

The PDE is 160 cm long with the first 100 cm of tube consisting of 3.81-cm-diam round tube. The last 60 cm consists of a 20 cm long, constant-area, round-to-square transition, followed by a 20 cm long square recovery section, followed by a 20 cm long, planar nozzle visualization section. The top and bottom surfaces of the nozzle section are removable, allowing arbitrary two-dimensional geometries to be tested. The L/D ratio is 42, as was the case for the parametric study.

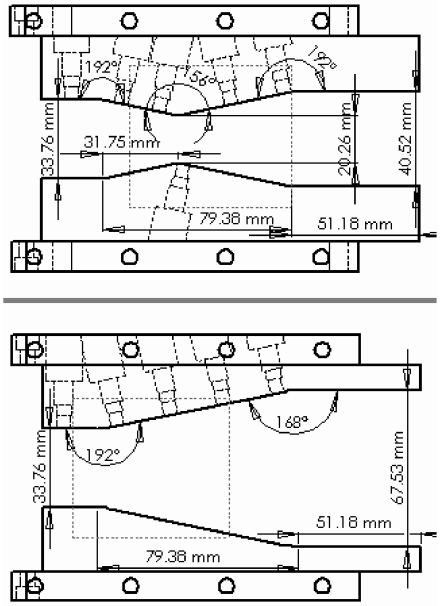

Fig. 6 Geometry for CD nozzle (top) and diverging nozzle (bottom). Nozzle width (into page) is constant and equal to 3.38 cm. The dotted square indicates viewable section during schlieren imaging.

For this study the facility is operated on a stoichiometric C_2H_4/O_2 mixture. The fuel and oxidizer are fed through choked orifices into a jet-in-crossflow mixer where they are premixed just upstream of the head-end injection point. The supply tank pressures of the fuel and oxidizer being fed to this mixer through choked orifices can be independently adjusted to change the stoichiometry of the charge. After mixing, the injection plumbing bifurcates and injection occurs at the top and bottom of the tube as illustrated in Fig. 7. The ignition of the premixed gases is initiated when the reactant charge has reached the exit of the tube where the arrival and stoichiometry can be monitored with a diode laser sensor (not shown) [32,33]. It is important to note that these experiments differ slightly from the parametric study because the reactants fully fill the nozzle section as opposed to having a nonreactive tamper mass in the nozzle. After filling is complete, the mixture is ignited with a 100 mJ electric spark which is located 6 cm from the head wall.

The deflagration-to-detonation transition (DDT) is measured using ion probes, and a fully established detonation wave takes approximately 30 cm to develop. At first the detonation wave is slightly overdriven, but the wave speed then decays and remains within 3% of the CJ value (2.4 km/s for stoichiometric C_2H_4/O_2) after passing the measurement station 60 cm from the tube head wall. Exhaust gases are discharged from the open end of the PDE into a large, continuously purged dump tank. In this study the tube is operated in single shot-mode only and all experimental results were conducted at $P_{\text{fill}} = P_{\text{atm}} = 1$ atm. It is important to understand when interpreting the experimental results that the magnitude of the measured values of thrust and I_{sp} would increase if the experiments had been conducted at a $P_{\text{fill}}/P_{\text{atm}}$ ratio greater than unity.

2. Impulse Measurement Setup

Time-resolved thrust measurements are made using wall-mounted pressure transducers in each nozzle, as shown in Fig. 6, as well as a transducer in the head wall. All pressure transducers are Kistler model 603B1 and each is connected to its own Kistler model 5010B charge amplifier.

Neglecting viscous effects, the instantaneous force vector acting on the engine during a single cycle can be determined by integrating the gauge wall pressure over the internal surface of the PDE as in Eq. (13):

$$\boldsymbol{F}(t) = \oiint_S P_{\text{wall}} \bar{\bar{I}} \cdot \boldsymbol{n}\, \mathrm{d}S \tag{13}$$

In these experiments it is assumed that wall pressure forces on the top and bottom nozzle surfaces are symmetric, and that the pressure measured at the center of the head wall acts uniformly over this surface. The x-component of the force vector (thrust) is of primary concern and consequently only measurements at the head wall and nozzle surfaces are required.

Single-cycle impulse is computed by integrating the thrust over the cycle time as shown in Eq. (10). The cycle time is defined, as before, to be the elapsed time from ignition until the head wall pressure has decayed to the ambient value. The single-cycle specific impulse is computed using Eq. (11).

When reducing the nozzle pressure data from the CD and diverging nozzles, rather then performing a coarse spatial integration using only the transducer locations as discrete elements, the pressure data are fit using monotone, Hermite interpolating polynomials. The fit is believed to increase the accuracy of the spatial integration within the nozzle and is performed separately on pressure data at each time level throughout the blowdown. The Hermite polynomials were chosen because they produce no overshoot between data points and were observed to maintain the expected curvature in the pressure profile throughout the cycle.

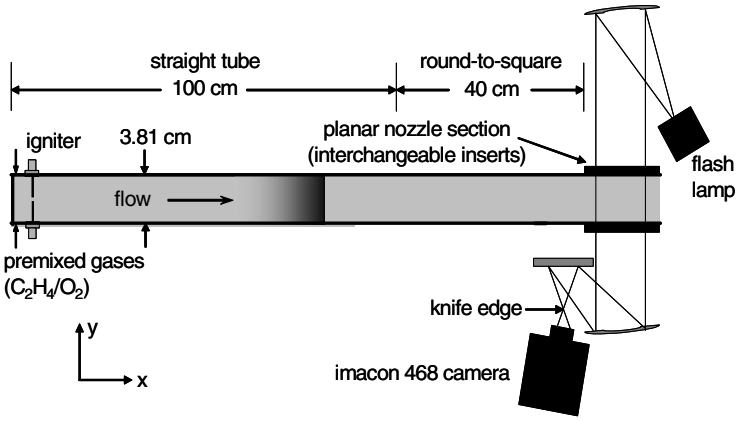

Fig. 7 Experimental PDE facility with planar, nozzle viewing chamber. Also shown is mirror-based, Z-arrangement schlieren imaging system.

3. Schlieren Imaging Setup

Figure 7 also shows the mirror-based, Z-arrangement schlieren system used for this study. The light source is a Hadland Photonics pulsed xenon flash lamp. The system has programmable pulse widths of 20, 50, and 200 μs with corresponding output energies of 125, 375, and 700 J, respectively. Nominally the 50 μs pulse width was used for this study. The Imacon 468 camera system, also manufactured by Hadland Photonics, consists of eight separately intensified CCD arrays (576×385), which are illuminated independently by an internal beam splitter which directs light onto each of the eight channels. The interframe timing and exposure of each channel can be independently adjusted from 10 ns to 1 ms. Internal camera timing events are controlled by a 100 MHz quartz crystal and output triggers are available to program external devices such as the pulsed xenon flash lamp.

Two 14-cm-diam, 61 cm focal length, parabolic mirrors were used to collimate light from the source and refocus the light on the camera side to the location of the knife edge. To consolidate the size of the setup a flat mirror was used in between the parabolic mirror and the knife edge. Unless otherwise noted, the knife edge was oriented vertically to provide sensitivity to density gradients along the nozzle x-axis.

The dotted square inside each insert in Fig. 6 indicates the viewable section of the nozzle. The windows for the nozzle section were made from 7.1 cm square, 1.25 cm thick sapphire. The hardness of the windows made them extremely resistant to scratching and proved to be a far superior choice over the polycarbonate windows which were used in preliminary experiments. In practice the windows needed to be cleaned after every 10 cycles as the large turbulent boundary layer present at the end of the cycle would leave deposits near the edges of the channel.

B. Thrust Measurement Results

Thrust measurements for all three nozzles will be presented along with the results computed using the quasi-one-dimensional model. For the purpose of accurate comparison the simulated results are computed using full finite-rate chemistry throughout the blowdown. The detonation wave is initiated using a 3000 K, 10 atm spark region occupying 1% of the tube volume centered at the igniter location. To avoid the computational expense of simulating the larger domain, each case is computed at 1/16 scale and the results are correspondingly rescaled in time by the same factor. This scaling procedure is predicated on the fact the model does not contain any diffusive terms, such as viscosity and thermal conduction, which would be sensitive to an absolute length scale. Also, because no attempt has been made to resolve the reaction zone, the chemical production rates do not need to be rescaled to preserve the ratio of the reaction zone to the length of the facility. This scaling procedure, used with the same chemical mechanism and grid resolution, has been used successfully in the past to simulate PDE parameters including velocity, temperature, and Y_{OH} in close agreement with experimental data [16,17].

Rather then discuss I_{sp} results in conjunction with the thrust measurements, this topic will be deferred until after the schlieren images for each nozzle insert have been discussed. The imaging results reveal several aspects of the flowfield which lend additional insight into the comparisons of I_{sp} between all nozzle cases. In this section the focus will be on trends in the thrust curves for each nozzle and how they differ from the simulated result.

1. Straight Tube

Straight-tube results are presented first because it represents the baseline case and will have several features in common with the other two nozzles. The first thing to observe in Fig. 8 is the difference between the simulation and the experiment at time-zero. At early times the simulation shows an instantaneous spike corresponding to direct initiation and then reflection of the detonation wave off the head wall. Recall that the igniter is actually offset from the head wall by 6 cm. In the experiment we observe a 0.3 ms delay before the head pressure begins to rise. The spark energy of our ignition system is not sufficient to generate direct initiation, thus the first experimental spike is the result of the left-running DDT process occurring between the spark location and the head wall. The second larger spike in the experimental plot results from the head wall reflection of a left-running shock wave that forms after the right-running detonation front has become established. This left-running shock wave is generated due to the large pressure differential between the CJ state and the relatively low-pressure wake occupying the DDT region.

Several attempts of limited success were made at crudely simulating this phenomenon by depositing less energy into the spark region, thereby delaying the coupling of the reaction zone with the lead shock. Whereas it was possible to capture the basic wave behavior of this process, the timings of the events were not in good agreement with experiment. The inability of the simulation to capture this early time phenomena is attributed to the lack of diffusion in the purely convective model. To model the DDT process, flame speed would have to be calculated accurately, which necessitates the inclusion of diffusive terms.

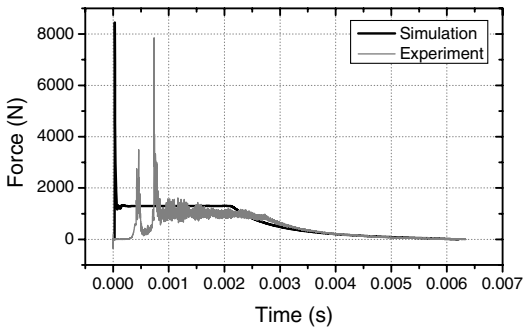

Fig. 8 Straight-tube thrust comparison of simulation vs experiment. Time-zero corresponds to ignition and the blowdown is terminated when $P_{head} = 1$ atm.

The second important discrepancy between the experiment and the model is with regard to the plateau force. For reasons already discussed, the plateau force will be longer in the simulation as a result of direct initiation. The effect this has on differences between computed and measured I_{sp} will be considered shortly. The magnitudes of the plateau regions are different as well. The plateau force observed in experiments is 24% lower than the computed result. In the past this discrepancy has been attributed to heat transfer effects, which are not accounted for in the model [34]. Another explanation includes accounting for the consequences of turbulence immediately following the reaction zone of a detonation wave, which were shown by White [35] to lead to lower pressure and density than the values predicted by CJ theory. The conclusive origins of this discrepancy are still unresolved.

2. *Converging-Diverging Nozzle*

In Fig. 9, as expected, the effects of direct initiation vs a finite DDT distance are again visible. Note that the spike in the experimental data at time-zero is caused by electromagnetic interference from the igniter and does not represent a pressure spike. The discrepancy in plateau force between experiment and simulation is also identical to that described for the straight-tube case. These effects will extend to the diverging nozzle as well and will not be discussed further.

For the CD nozzle considered here we see that the thrust augmentation provided by the diverging section is nearly identically canceled by the thrust reduction caused by the converging section during early times after the detonation wave has passed through the nozzle. However, while the diverging section quickly decays to nearly zero thrust, the converging section continues to negatively impact the total impulse throughout much of the cycle. Close examination of Fig. 9 reveals that the diverging thrust only goes negative very near the end of the cycle, a characteristic common to the optimal designs in the parametric study. This provides confidence that the selected expansion area ratio is likely near the optimal point.

In Fig. 10 the total thrust for the CD nozzle is plotted as a function of time. In this plot the simulated data have been shifted forward so that detonation arrival at the nozzle (indicated by the spike near 1 ms) coincides with the experimental data. In general the model reproduces the experimental trends well; however, the magnitude of all features is higher than observed in experiments. Interestingly, even after the arrival times of the detonation waves at the nozzle section have been aligned, we see that the arrival of the reflected shock at the head wall occurs slightly sooner in the simulation than it does in experiments. This discrepancy of wave arrival time is attributed to a higher acoustic speed in the wake of the detonation for the simulation as compared to the experiment. This phenomenon is discussed in [16], which attributes the reduced mean acoustic speed

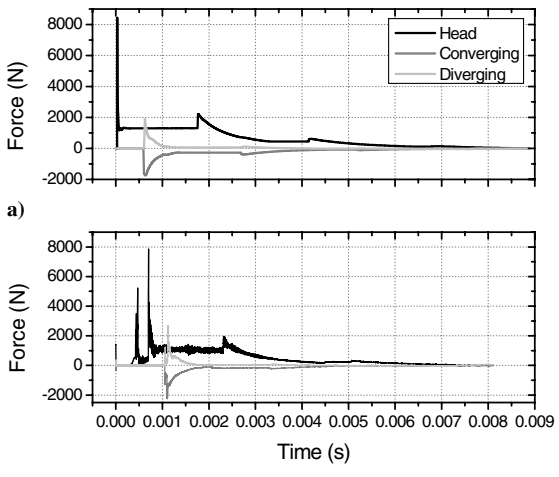

Fig. 9 Converging-diverging nozzle component thrust comparison of a) simulation vs b) experiment. Time-zero corresponds to ignition and the blowdown is terminated when $P_{\text{head}} = 1$ atm.

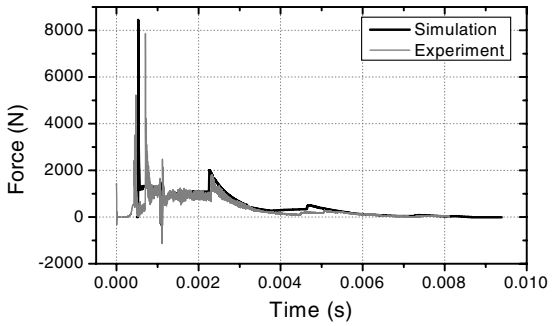

Fig. 10 Converging-diverging nozzle total thrust comparison of simulation vs experiment. The arrival of the detonation wave at the nozzle has been used to align the features in each plot. Time-zero corresponds to ignition in the experimental data only.

in the wake region to heat loss effects not accounted for in the model. This same explanation accounts for the early arrival of the second smaller wave reflection occurring at 5 ms as evident in Fig. 10.

3. *Diverging Nozzle*

In Fig. 11 the thrust components for the diverging nozzle are plotted as a function of time. We see a significant contribution to impulse from the diverging section in this plot. As was the case for CD nozzle, careful examination of Fig. 11 reveals that the force on the diverging section only becomes slightly negative at the end of the cycle. This again is a characteristic common to the optimal designs in the parametric study. The fact that both nozzle experiments show an expansion area ratio of 2 to be near the optimal point confirms the conclusion that optimal expansion ratio is not strongly sensitive to the level of throat obstruction.

In Fig. 12 the total thrust for the diverging nozzle is plotted vs time. As before, the arrival of the detonation wave at the nozzle section for the simulated case has been aligned with the experimentally observed arrival time. Again we see the ability of the model to reproduce the correct trends in thrust, however, at a magnitude higher than that observed in the experiment. For the case of the diverging nozzle, which has a very short blowdown time, the total impulse is heavily weighted towards the contribution from the plateau region. Consequently, the ability to predict impulse performance for a diverging nozzle is largely dependent on predicting the plateau conditions at the head end with high accuracy.

C. Schlieren Imaging Results

To aid in the comparison of simulated to experimental data, schlieren imaging was performed on all three nozzle inserts. During a

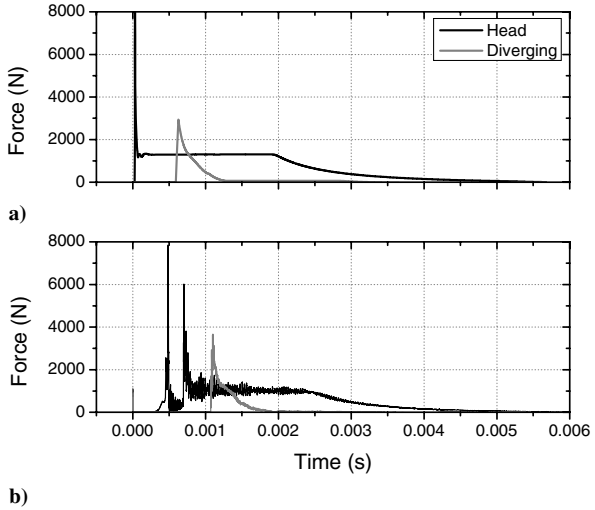

Fig. 11 Diverging nozzle component thrust comparison of a) simulation vs b) experiment. Time-zero corresponds to ignition and the blowdown is terminated when $P_{\text{head}} = 1$ atm.

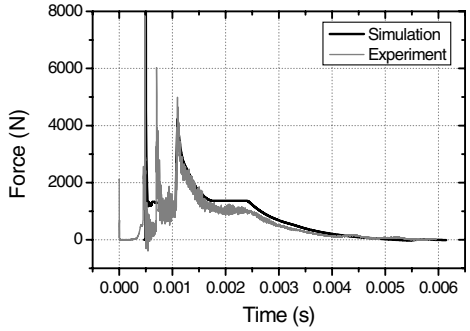

Fig. 12 Diverging nozzle total thrust comparison of simulation vs experiment. The arrival of the detonation wave at the nozzle has been used to align the features in each plot. Time-zero corresponds to ignition in the experimental data only.

single run the light source was programmed for a 50 μs pulse, and during this time up to eight separate exposures could be taken. To image the entire blowdown process many runs were necessary and to ensure repeatability the first and last frames of consecutive runs were overlapped. For the CD and diverging nozzles the camera was triggered using the first pressure transducer in the nozzle section. Using this procedure resulted in excellent repeatability because the duration of the DDT process is the least repeatable event, and this took place before the camera was triggered. More care needed to be taken with the straight-tube configuration because a transducer port was not available close to the nozzle. In this section we will focus the discussion on blowdown gasdynamics and defer its relevance to I_{sp} prediction until the final section.

1. *Straight Tube*

In Fig. 13 an 18-frame schlieren imaging sequence is shown beginning with the arrival of the detonation wave in the nozzle section and concluding with fully turbulent channel flow at the end of the cycle. From 1.07 to 1.08 ms we see the detonation front entering and traversing to the center of the viewable section. Behind the detonation front we see a series of intersecting oblique shock waves which are stationary relative to the detonation front. The existence of this oblique pattern has been observed previously by Edwards et al. [36], and their origin still remains uncertain. An especially intriguing result arising due to the existence of this wave pattern is that flow in this region must be supersonic relative to the detonation front. According to CJ theory this would require the detonation wave to exist on the weak branch of the Rankine–Hugoniot curve which is forbidden by conventional entropy arguments. However, the turbulent structure hypothesis of White [35], which was referenced previously as an explanation for the decreased pressure in the plateau region, also predicts the existence of supersonic flow behind the detonation front. In his paper, White shows that the addition of turbulent terms to the conservation equations precludes the existence of an exact CJ state as defined by the point of tangency between the Rankine–Hugoniot and the Rayleigh line. Once the tangency condition is removed, the arguments that support the inexistence of weak detonations become invalid. White's postulation is neither confirmed nor denied in this study.

Using White's hypothesis, Edwards et al. [36] suggest the oblique shock pattern is formed because of a large pressure gradient across the boundary layer in the reaction zone behind the detonation front. The pressure gradient is established because the reaction rate in the boundary layer is slower than that of the core flow, thus maintaining the boundary layer closer to the von Neumann pressure, whereas the core flow has reacted sufficiently to approach the CJ state. Provided the flow is supersonic relative to the detonation front, this pressure differential would cause sufficient perturbation to generate the oblique shock pattern observed in Fig. 13.

Whatever the cause of the oblique shock pattern, it is clear that the strong reflected shock which comes into view at 1.085 ms is preventing the pattern from propagating further upstream. This strong reflected normal shock was described previously and is generated by the large pressure differential established between the flow behind the right-moving detonation front and the low-pressure wake in the DDT region. This wave is traveling extremely fast, as it was initially translating towards the head wall before it reflected and proceeded to nearly catch up to the detonation wave in the nozzle section.

After the detonation wave and reflected normal shock have exited the tube, a brief period of shock-free flow is established until at 1.5 ms a set of left-moving oblique shocks translate upstream, most likely resulting from the diffraction of the exiting detonation wave. Because of the orientation of the knife edge, left-moving shocks will appear lighter and right-moving shocks will appear darker. These structures reside in the nozzle section until they move out of the left edge at 1.62 ms. The blowdown continues until at 5 ms, turbulent boundary layer separation begins to occur along the top and bottom surfaces of the channel. By 7 ms the channel flow has become fully turbulent. Simulation results suggest that reverse flow, or suction of exhaust gases back into the tube, does not occur until several milliseconds after the last frame shown. The turbulent channel flow is suspected to arise when the boundary layer flow separates due to an adverse pressure gradient which begins to form at the end of the cycle before reverse flow.

2. *Converging-Diverging Nozzle*

In Fig. 14 the passage of the detonation wave through the CD nozzle with the knife edge oriented horizontally is shown. The viewable portion of CD nozzle was indicated in Fig. 6. The knife edge has been rotated to this orientation to resolve the system of transverse reflections occurring due to the interaction of the detonation wave with the converging section. The knife edge is positioned in such a fashion that upward-moving shocks will appear lighter whereas downward-moving shocks will appear darker.

We see in Fig. 14 that the passage of the detonation through the converging section generates two strong opposing shock waves

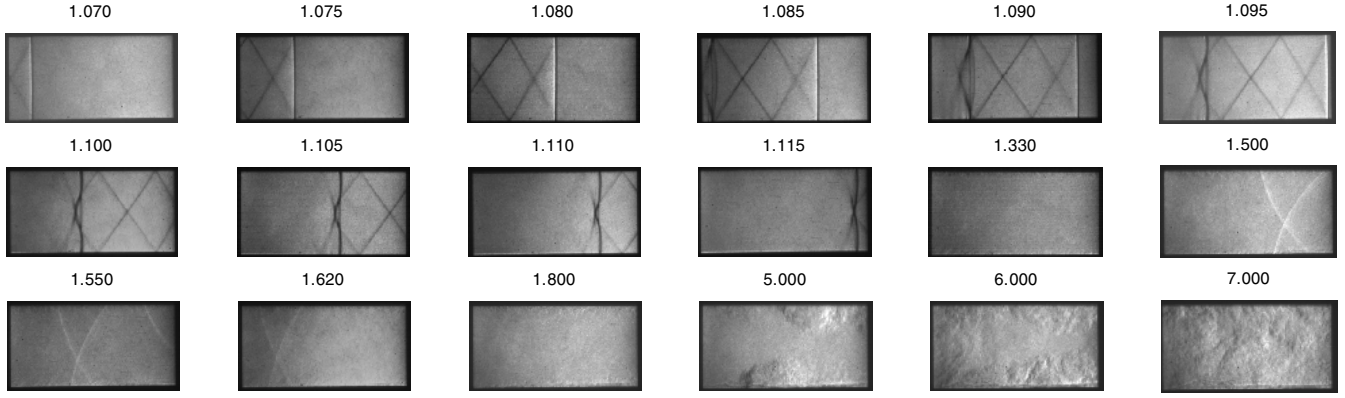

Fig. 13 Straight-tube blowdown image sequence. Numbers above each frame indicate time in milliseconds from ignition. Knife edge is oriented vertically such that right-moving shocks appear darker.

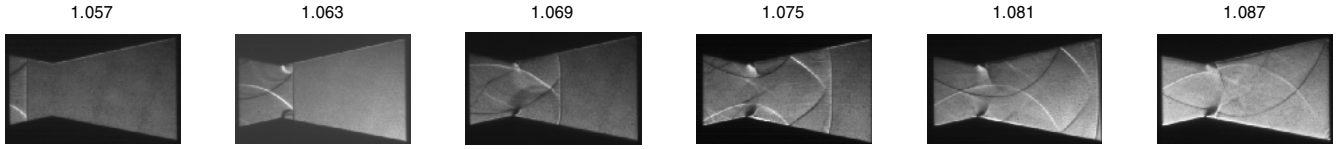

Fig. 14 Converging-diverging nozzle detonation passage sequence. Numbers above each frame indicate time in milliseconds from ignition. Knife edge is oriented horizontally such that downward-moving shocks appear darker.

which intersect each other and proceed to reflect transversely back-and-forth across the nozzle section. Note that these transverse waves prevent the occurrence of the oblique shock pattern observed in the straight tube. Because of the curvature of these waves and the presence of the diverging section, the downstream part of the same reflected wave will complete its second reflection before the upstream part. This leads to the inflection point visible near the center of the 1.075 ms frame. Strong expansion fans emanating from the throat section indicate the presence of choked flow in the nozzle immediately after detonation passage. The asymmetry of the shading of these expansion fans across the nozzle section is due to the horizontal knife edge orientation. Careful examination of the 1.063 and 1.069 ms frames also reveals the propagation of small acoustic disturbances from the location of the pressure transducer ports.

The first six frames of Fig. 15 were taken at identical times to those in Fig. 14 with the only difference being the orientation of the knife edge, which is vertical for the later figure. The vertical knife edge orientation reveals several new slip lines and also makes the reflected normal shock visible.

After the reflected shock exits the nozzle at 1.102 ms, the unsteady starting process begins. The 1.122 ms frame reveals a system of oblique shock waves coalescing into a normal shock at the intersection of the lead Mach waves emanating from the expansion fan. Just downstream of this feature two additional oblique shock waves form at the walls of the diverging channel. The upstream feature develops into a normal shock which is pushed downstream and merges with the second shock system, forming a single strong normal shock near the exit of the nozzle as shown in the 1.192 ms frame. Strong, turbulent flow separation is evident behind this shock structure. After 1.487 ms the normal shock weakens and is pushed out of the nozzle at 1.587 ms. Shock-free flow is present in the nozzle until at 4.237 ms turbulent boundary layer separation begins to occur in the diverging section. At 5.237 ms a normal shock wave is just visible in the turbulent region at the exit of the nozzle. As part of the nozzle unstarting process the normal shock is sucked upstream and through the throat at which point the nozzle unchokes and becomes fully turbulent at 8.237 ms.

3. *Diverging Nozzle*

In Fig. 16 the blowdown sequence for the diverging nozzle is shown. The oblique shock pattern is again present in this case until it is quenched by the arrival of the reflected shock at 1.075 ms. Expansion waves are evident at the start of the diverging section immediately after the passage of the detonation wave (1.065 ms), indicating choked flow. After the reflected shock exits the tube at 1.093 ms, the nozzle starting process begins. At 1.137 ms two oblique shock waves form just downstream of the expansion fan. Similar to the CD nozzle, at 1.207 ms the aforementioned oblique shock waves have coalesced into a normal shock which is pushed downstream and merges with the second shock structure present at the exit to form a single strong normal shock. Again, the presence of turbulent, separated flow behind the normal shock is evident. Interestingly, at 1.437 ms two weaker oblique shock structures are again visible and proceed to intersect at 1.497 ms before a normal shock forms and is expelled from the nozzle at 1.687 ms. It appears the downstream oblique shock structure at 1.437 ms may again be the result of detonation diffraction at the tube exit. Shock-free flow persists in the nozzle until at 4.597 ms two oblique waves form at exit of the nozzle, inducing turbulent separated flow. The unstarting process progresses with the normal shock being sucked into the throat at 5.077 ms, after which the flow proceeds to become fully turbulent in the nozzle section.

D. Specific Impulse Results

The discussion of simulated vs measured specific impulse with regard to each of the three nozzle configurations has been deferred until now so that the results can be considered in light of the flow visualization results. Uncertainty estimates given for the measured values of I_{sp} are computed based on the standard deviation between all values in the data set used to construct the mean values presented in Table 1.

It is of interest to compare the magnitude of the results given for the straight tube in Table 1 to those readily available in previous studies. The computed straight-tube I_{sp} of 178 s agrees exactly with the results presented in [18]. The experimental result for the straight tube differs notably from that presented by Cooper et al. [37]. This discrepancy is a result of the definition of t_{cycle}. In ballistic pendulum-based impulse measurements made by Cooper et al., no explicit definition of t_{cycle} is required and a resulting I_{sp} of 170 s is recorded for the stoichiometric, C_2H_2/O_2, straight tube. For reasons of practical applicability in multipulse PDEs, where operating frequency is to remain high, we define the end of a cycle as the

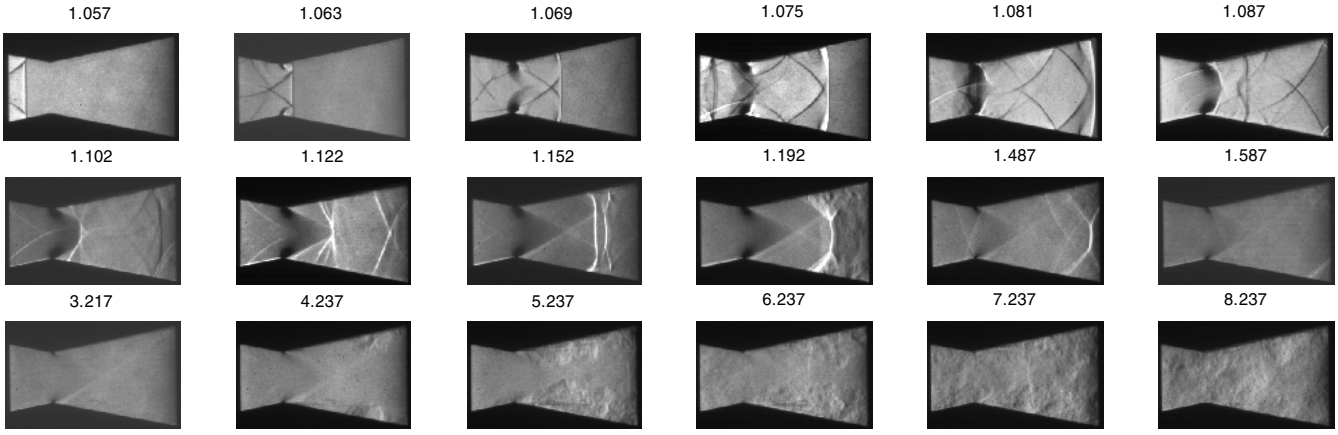

Fig. 15 Converging-diverging nozzle blowndown image sequence. Numbers above each frame indicate time in milliseconds from ignition. Knife edge is oriented vertically such that right-moving shocks appear darker.

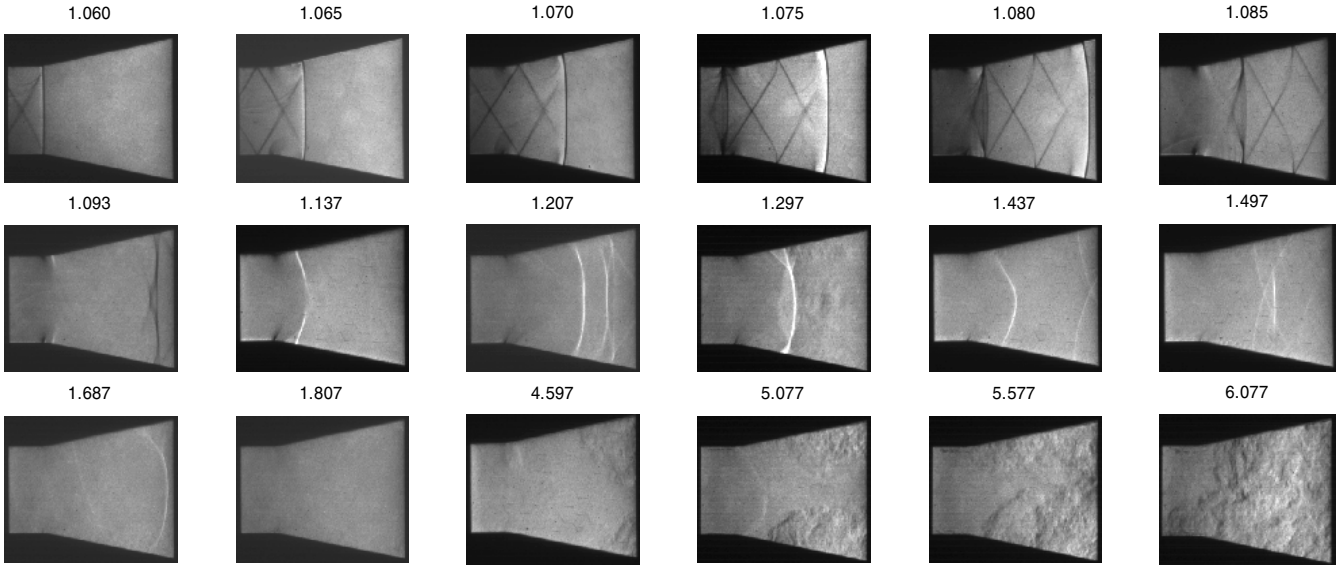

Fig. 16 Diverging nozzle blowdown image sequence. Numbers above each frame indicate time in milliseconds from ignition. Knife edge is oriented vertically such that right-moving shocks appear darker.

time when P_{head} has decayed to P_{atm}. If the integration of total impulse is extended to long times, then a value of 165 ± 7 s is determined. This result is in agreement with the measurement in [37]. The additional impulse at the end of t_{cycle} is the result of a small reflecting wave which persists in the PDE chamber even at long times due to the self-aspirating nature of the PDE blowdown process [1]. This wave results in a small head wall compression above the ambient pressure after each reflection.

The results in Table 1 confirm several results presented in the parametric study. For a single cycle the measured I_{sp} for the diverging nozzle is unequivocally higher than for the CD nozzle and the straight tube. This confirms that a diverging nozzle with a nearly optimal expansion area ratio can outperform the straight-tube case even at high backpressure. Additionally, we see that the nearly optimally expanded CD nozzle at least matches, if not exceeds, the impulse generated by the straight tube.

For all three nozzles, the single-cycle blowdown time predicted by the quasi-one-dimensional model is within 10% of the experimental value. This suggests that the turbulent structure and viscous nozzle separation phenomena occurring near the end of the blowdown do not need to be resolved to make an accurate prediction of blowdown time.

The simulated total I_{sp} data presented in Table 1 are in all preceding cases that observed in the experiment. The I_{sp} for the straight tube is overpredicted by 28%, the CD nozzle by 25%, and the diverging nozzle by 20%. These discrepancies are the result of several effects. The first effect is that the simulations undergo direct initiation whereas the experiments do not. To quantify the effect of direct initiation on I_{sp}, the additional plateau region, occurring in the simulated results, was subtracted and the I_{sp} was recomputed. The result revealed that in each case 7–9% of the cited discrepancy can be attributed to direct initiation. The remaining disagreement can be largely attributed to the inability of the model to correctly capture the plateau pressure. As discussed previously, this could potentially be a heat transfer effect or a result of White's turbulent structure hypothesis [35].

Another effect, which merits special attention for 1-D simulations, is the effect of the exit boundary condition on the resulting impulse. As discussed in [28], the treatment of the exit boundary can have a significant impact on the rate at which the pressure in the plateau region relaxes back to the ambient value. In the case of the straight-tube configuration it is possible that some discrepancy can be attributed to the zero-relaxation-length pressure boundary condition (used for subsonic outflow), and the specification of sonic flow directly at the exit plane (used for supersonic outflow). This effect is expected to be minor, considering the general shape of the experimental relaxation observed in Fig. 8 is captured well by the model. The role of the boundary condition for the CD and diverging nozzles is also expected to have very little impact on the resulting impulse. In both of these nozzles the flow remains supersonic at the exit throughout the first 80% of the cycle, and during this time the boundary condition is entirely determined by the internal domain. As evident in Figs. 9 and 11, during the last 20% of the cycle very little is contributed to the total impulse and the zero-relaxation-length pressure boundary condition is not expected to have an appreciable effect.

Table 1 also reveals a large deviation between measured and computed values of head and converging section I_{sp} for the CD nozzle. The fact that the predicted total I_{sp} deviates from the experiment to the same extent as the other two cases is fortuitous because the overprediction at the head wall is offset by the overprediction at the convergent section. This deviation is due to the inaccuracy of the quasi-one-dimensional model in predicting a wave reflection event which is truly multidimensional. As evident in Figs. 14 and 15, a large fraction of the energy from the detonation wave reflection off of the convergent section goes into the system of

Table 1 Comparison of measured and computed single-cycle I_{sp} for each nozzle. Simulations are performed with direct initiation whereas experiments have a finite DDT distance. The total impulse used to evaluate each I_{sp} is evaluated over a single t_{cycle}. ($P_{\text{fill}} = P_{\text{amb}} = 1$ atm)

Nozzle insert	I_{sp} head, s	I_{sp} converging, s	I_{sp} diverging, s	I_{sp}, s	t_{cycle}, ms
Straight (exp)	140	0	0	140 ± 5	6.3
Straight (sim)	178	0	0	178	6.2
CD (exp)	167	−41	15	141 ± 5	8.2
CD (sim)	226	−62	13	177	8.9
Diverging (exp)	131	0	28	159 ± 5	6.0
Diverging (sim)	163	0	26	189	5.7

transverse waves reflecting back-and-forth across the nozzle channel. The reflection of these waves off the nozzle surface produces only a small thrust component in the axial direction. This would account for why the measured convergent I_{sp} is much lower in absolute magnitude than the simulated value. This same effect also controls the strength of the reflected wave which travels back towards the head wall. The quasi-one-dimensional model is predicting much too strong of a reflected wave because much of this energy is in reality lost in the formation of the transverse shock waves.

The diverging section I_{sp} is well predicted for both the CD and diverging nozzles because the impulse here is not strongly dependent on accurate resolution of any axial shock reflections. The fact that experimental value is actually slightly higher than the simulated value in the diverging section suggests that the transverse wave phenomenon that goes unresolved in the quasi-one-dimensional model may actually have a detectable effect on the impulse.

V. Conclusions

A quasi-one-dimensional, Euler model, with detailed finite-rate kinetics was used to study the effects of area ratio on unsteady nozzle performance in a PDE. The results indicate that the contraction area ratio, which largely controls the duration of a single cycle as well as the average pressure and Mach number of the gases at the end of the cycle, will ultimately need to be designed using a detailed multicycle analysis model. In general, due to the necessity to maintain high reactant fill pressures and the superior single-cycle performance of diverging nozzles, it is expected that the optimal contraction area ratio will have the minimum throat obstruction required to achieve the desired reactant state between cycles. Alternative refilling schemes will be an important area of future investigation because the magnitude of the performance enhancement provided by nozzles is critically dependent on achieving a high value of $P_{\text{fill}}/P_{\text{atm}}$.

Results from the parametric study indicate that the optimal expansion area ratio can be identified accurately by performing an isentropic analysis based on the time-averaged, head wall stagnation pressure for a given PDE geometry. This stagnation pressure is most strongly a function of the contraction area ratio; however, it was shown that the $P_{o,\text{avg}}$ value from the straight tube provides a valid reference point for approximating optimal expansion area ratios even for nozzle geometries with contraction ratios other than unity.

Time-resolved impulse measurements were made at each thrust surface and compared with simulation results. The largest deviations between simulated and experimental results are due to the inability of the model to capture the DDT event and the exact plateau pressure behind the detonation front. Model idealizations accounting for these discrepancies are discussed.

The nozzle performance trends highlighted in the simulation results are consistent with findings in the experimental data. We observe that appropriately optimized nozzles can be designed to outperform the straight-tube geometry even at high backpressures. In accordance with the parametric study, experimental data reveal that an optimized diverging nozzle produces the highest single-cycle I_{sp}.

Schlieren imaging of the blowdown event was performed in three separate nozzle geometries. The results of the imaging in comparison to impulse data reveal that whereas the quasi-one-dimensional model adequately captures the essential gasdynamics in straight tubes and diverging nozzles, it is less adept at capturing the magnitude of shock wave reflections occurring in nozzles with a convergent section. This deficiency results from the inability of the model to resolve the 2-D nature of the wave structure visible in the schlieren images. Fortuitously, the overprediction of the negative impulse on the convergent section is nearly canceled by a corresponding overprediction of the impulse at the thrust wall.

Acknowledgments

The authors would like to thank The Office of Naval Research and Gabriel Roy (technical monitor) for supporting this research. Additional acknowledgment should be given to Ethan Barbour, Dan Mattison, Ben Gauthier, Chris Morris, and Matei Radulescu for valuable discussions regarding the content of this work.

References

[1] Bussing, T., and Pappas, G., "An Introduction to Pulse Detonation Engines," AIAA Paper 1994-0263, 1994.

[2] Wu, Y., Ma, F., and Yang, V., "System Performance and Thermodynamic Cycle Analysis of Airbreathing Pulse Detonation Engines," *Journal of Propulsion and Power*, Vol. 19, No. 4, 2003, pp. 556–567.

[3] Heiser, W., and Pratt, D., "Thermodynamic Cycle Analysis of Pulse Detonation Engines," *Journal of Propulsion and Power*, Vol. 18, No. 1, 2002, pp. 68–76.

[4] Talley, G., and Coy, E., "Constant Volume Limit of Pulsed Propulsion for a Constant γ Ideal Gas," *Journal of Propulsion and Power*, Vol. 18, No. 2, 2002, pp. 400–406.

[5] Witenberger, E., and Shepherd, J., "Model for the Performance of Air-Breathing Pulse Detonation Engines," *Journal of Propulsion and Power*, Vol. 22, No. 3, 2006, pp. 593–603.

[6] Kailasanath, K., "A Review of Research on Pulse Detonation Engine Nozzles," AIAA Paper 2001-3932, 2001.

[7] Kailasanath, K., "Recent Developments in the Research on Pulse Detonation Engines," *AIAA Journal*, Vol. 41, No. 2, 2003, pp. 145–159.

[8] Cooper, M., and Shepherd, J. E., "The Effect of Transient Nozzle Flow on Detonation Tube Impulse," AIAA Paper 2004-3914, 2004.

[9] Morris, C. I., "Numerical Modeling of Single-Pulse Gasdynamics and Performance of Pulse Detonation Rocket Engines," *Journal of Propulsion and Power*, Vol. 21, No. 3, 2005, pp. 527–538.

[10] Morris, C. I., "Axisymmetric Modeling of Pulse Detonation Rocket Engines," AIAA Paper 2005-3508, 2005.

[11] Ma, F., Choi, J. Y., and Yang, V., "Thrust Chamber Dynamics and Propulsive Performance of Single-Tube Pulse Detonation Engines," *Journal of Propulsion and Power*, Vol. 21, No. 3, 2005, pp. 512–526.

[12] Yungster, S., "Analysis of Nozzle and Ejector Effects on Pulse Detonation Engine Performance," AIAA Paper 2003-1316, 2003.

[13] Cambier, J. L., and Tegner, J. K., "Strategies for Pulsed Detonation Engine Performance Optimization," *Journal of Propulsion and Power*, Vol. 14, No. 4, 1998, pp. 489–498.

[14] Paxon, D., "Optimal Area Profiles for Ideal Single Nozzle Air-Breathing Pulse Detonation Engines," AIAA Paper 2003-4512, 2003.

[15] Guzik, S. M., and Harris, P. G., "An Investigation of Pulse Detonation Engine Configurations Using the Method of Characteristics," AIAA Paper 2002-4066, 2002.

[16] Owens, Z., Mattison, D., Barbour, E., Morris, C., and Hanson, R., "Flowfield Characterization and Simulation Validation of Multiple-Geometry PDEs Using Cesium-Based Velocimetry," *Proceedings of the Combustion Institute 30*, The Combustion Institute, Pittsburgh, PA, 2005, pp. 2791–2798.

[17] Mattison, D., Oehlschlaeger, M., Morris, C., Owens, Z., Barbour, E., Jeffries, J., and Hanson, R., "Evaluation of Pulse Detonation Engine Modeling Using Laser-Based Temperature and OH Concentration Measurements," *Proceedings of the Combustion Institute 30*, 2005, pp. 2879–2807.

[18] Barbour, E., Owens, Z., Morris, C., and Hanson, R., "The Impact of a Converging-Diverging Nozzle on PDE Performance and its Associated Flowfield," AIAA Paper 2004-867, 2004.

[19] Kee, R. J., Rupley, F. M., and Miller, J. A., "Chemkin-II: A FORTRAN Chemical Kinetics Package for the Analysis of Gas-Phase Chemical Kinetics," Sandia National Laboratories, Tech. Rept. SAND89-8009, 1989.

[20] Varatharajan, B., and Williams, F. A., "Ethylene Ignition and Detonation Chemistry, Part 2: Ignition Histories and Reduced Mechanisms," *Journal of Propulsion and Power*, Vol. 18, No. 2, 2002, pp. 352–362.

[21] Strang, G., "On the Construction and Comparison of Difference Schemes," *SIAM Journal on Numerical Analysis*, Vol. 5, No. 3, 1968, pp. 506–517.

[22] Fedkiw, R. P., "A Survey of Chemically Reacting Compressible Flows," Ph.D. Dissertation, Dept. of Mathematics, Univ. of California, Los Angeles, Los Angeles, 1997.

[23] Aslam, T., "A Level-Set Algorithm for Tracking Discontinuities in Hyperbolic Conservation Laws," *Journal of Computational Physics*, Vol. 167, No. 2, 2001, pp. 413–438.

[24] Shi, J., Zhang, Y. T., and Shu, C. W., "Resolution of High Order WENO Schemes for Complicated Flow Structures," *Journal of Computational Physics*, Vol. 186, No. 2, 2003, pp. 690–696.

[25] Patrick, J., "On the Numerical Solution of the Compressible Navier-Stokes Equations for Reacting and Non-Reacting Gas Mixtures," Ph.D. Dissertation, Swiss Federal Institute of Technology, Zurich, Diss ETH No. 12030, 1997.

[26] Gottlieb, S., and Shu, C. W., "Total Variation Diminishing Runge-Kutta Schemes," *Mathematics of Computation*, Vol. 67, No. 221, 1998, pp. 73–85.

[27] Baum, M., Poinsot, T., and Thevenin, D., "Accurate Boundary Conditions for Multicomponent Reactive Flows," *Journal of Computational Physics*, Vol. 116, No. 2, 1994, pp. 247–261.

[28] Kailasanath, K., and Patnaik, G., "Performance Estimates of Pulsed Detonation Engines," *Proceedings of the Combustion Institute 28*, 2000, pp. 595–601.

[29] Reynolds, W. C., "The Element Potential Method for Chemical Equilibrium Analysis: Implementation in the Interactive Program STANJAN, Ver. 3," Stanford University TR A-3991, Department of Mechanical Engineering, Stanford, CA, 1986.

[30] Yungster, S., and Radhakrishnan, K., "Pulsating One-Dimensional Detonations in Hydrogen-Air Mixtures," *Combustion Theory and Modeling*, Vol. 8, No. 4, 2004, pp. 745–770.

[31] Witenberger, E., Austin, J., Cooper, M., Jackson, S., and Shepherd, J. E., "An Analytical Model for the Impulse of a Single-Cycle Pulse Detonation Engine," *Journal of Propulsion and Power*, Vol. 19, No. 1, 2003, pp. 22–38.

[32] Barbour, E., Ma, L., Jeffries, J., Hanson, R., Brophy, C., and Sinibaldi, J., "Real-Time Measurements of C_2H_4 Concentration with Application to PDEs Operating on Oxygen and Air," AIAA Paper 2005-4376, 2005.

[33] Ma, L., Sanders, S., Jeffries, J., and Hanson, R., "Monitoring and Control of a Pulse Detonation Engine Using a Diode-Laser Fuel Concentration and Temperature Sensor," *Proceedings of Combustion Institute 29*, 2002, pp. 161–166.

[34] Radulescu, M. I., and Hanson, R. K., "Effect of Heat Loss on Pulse-Detonation-Engine Flow Fields and Performance," *Journal of Propulsion and Power*, Vol. 21, No. 2, 2005, pp. 274–285.

[35] White, D. R., "Turbulent Structure of Gaseous Detonation," *Physics of Fluids*, Vol. 4, No. 4, 1961, pp. 465–480.

[36] Edwards, D. H., Jones, T. G., and Price, B., "Observations of Oblique Shock Waves in Gaseous Detonations," *Journal of Fluid Mechanics*, Vol. 17, Pt. 1, 1963, pp. 21–34.

[37] Cooper, M., Jackson, S., Austin, J., Witenberger, E., and Shepherd, J. E., "Direct Experimental Impulse Measurements for Detonations and Deflagrations," *Journal of Propulsion and Power*, Vol. 18, No. 5, 2002, pp. 1033–1041.

J. Powers
Associate Editor